A scanning focus nuclear microscope with multi-pinhole collimation

Nguyen, Minh Phuong; Arif, Muhammad; Oostenrijk, Bart; Goorden, Marlies C.; Beekman, Freek J.

DOI
10.1088/1361-6560/acbf9b

Publication date
2023

Document Version
Final published version

Published in
Physics in medicine and biology

Physics in Medicine & Biology

PAPER • **OPEN ACCESS**

A scanning focus nuclear microscope with multi-pinhole collimation

To cite this article: Minh Phuong Nguyen *et al* 2023 *Phys. Med. Biol.* **68** 075010

IOP Publishing Phys. Med. Biol. 68 (2023) 075010 https://doi.org/10.1088/1361-6560/acbf9b

Physics in Medicine & Biology

IPEM Institute of Physics and Engineering in Medicine

OPEN ACCESS

RECEIVED
25 October 2022

REVISED
8 February 2023

ACCEPTED FOR PUBLICATION
27 February 2023

PUBLISHED
23 March 2023

PAPER

A scanning focus nuclear microscope with multi-pinhole collimation

Minh Phuong Nguyen[1,2,3,4,*], **Muhammad Arif**[2,4], **Bart Oostenrijk**[1], **Marlies C Goorden**[2] and **Freek J Beekman**[1,2]

[1] MILabs BV, Houten, The Netherlands
[2] Section Biomedical Imaging, Delft University of Technology, Delft, The Netherlands
[3] Delft University of Technology, Mekelweg 5, 2628 CD Delft, The Netherlands
[4] These authors contributed equally to this work.
[*] Author to whom any correspondence should be addressed.

E-mail: m.nguyen@milabs.com

Keywords: nuclear microscope, high resolution, SPECT, pinhole, collimator

Abstract

Microscopic nuclear imaging down to spatial resolutions of a few hundred microns can already be achieved using low-energy gamma emitters (e.g. ^{125}I, ~30 keV) and a basic single micro-pinhole gamma camera. This has been applied to *in vivo* mouse thyroid imaging, for example. For clinically used radionuclides such as ^{99m}Tc, this approach fails due to penetration of the higher-energy gamma photons through the pinhole edges. To overcome these resolution degradation effects, we propose a new imaging approach: scanning focus nuclear microscopy (SFNM). We assess SFNM using Monte Carlo simulations for clinically used isotopes. SFNM is based on the use of a 2D scanning stage with a focused multi-pinhole collimator containing 42 pinholes with narrow pinhole aperture opening angles to reduce photon penetration. All projections of different positions are used to iteratively reconstruct a three-dimensional image from which synthetic planar images are generated. SFNM imaging was tested using a digital Derenzo resolution phantom and a mouse ankle joint phantom containing ^{99m}Tc (140 keV). The planar images were compared with those obtained using a single-pinhole collimator, either with matched pinhole diameter or with matched sensitivity. The simulation results showed an achievable ^{99m}Tc image resolution of 0.04 mm and detailed ^{99m}Tc bone images of a mouse ankle with SFNM. SFNM has strong advantages over single-pinhole imaging in terms of spatial resolution.

1. Introduction

Preclinical nuclear imaging is an important tool in biomedical research to monitor biological functions inside small experimental animals or tissue samples. In the past, this type of imaging most often required cryo-cooling and sectioning of the animal or tissue sample followed by autoradiography or other counting assays. Nowadays, the whole subject can be scanned by a dedicated positron emission tomography (PET) scanner in the case of positron emitters or by a position-sensitive gamma-radiation detector equipped with a collimator for the study of single-photon and positron emitter distributions in either planar or tomographic mode (SPECT). Preclinical planar imaging and physically collimated tomography both have an advantage over preclinical coincidence PET in terms of achievable image resolution; thanks to the use of magnified pinhole imaging, the achievable image resolution can typically be more than an order of magnitude better than the intrinsic detector spatial resolution (typically 3.5 mm for conventional large-area gamma cameras) (Beekman and Van Der Have 2007). Various preclinical pinhole SPECT systems are now available on the market (Furenlid *et al* 2004, Beekman *et al* 2005, Kim *et al* 2006, Schramm *et al* 2006, Hesterman *et al* 2007, van der Have *et al* 2009, Sánchez *et al* 2013, Ivashchenko *et al* 2015, Nguyen *et al* 2020a), offering image resolutions down to 250 μm *in vivo* (Ivashchenko *et al* 2015) and 120 μm *ex vivo* (Nguyen *et al* 2020b).

In an attempt to work towards *in vivo* nuclear microscopy, a micro-pinhole with a 100 μm aperture was previously used in a compact bench-top camera. Measured projections through this pinhole demonstrated

high-resolution imaging with low-energy gamma-emitting isotopes (e.g. ^{125}I, ~30 keV) (Beekman *et al* 2002). This single-pinhole (SPH) approach falls short when imaging clinically used isotopes such as ^{99m}Tc (140 keV) due to severe photon penetration through pinhole edges that degrades image quality. One of the approaches to reduce pinhole edge penetration is to utilise multiple pinholes with smaller pinhole openings (Goorden and Beekman 2010, Könik *et al* 2019).

With multiple pinholes, it is not straightforward to obtain an image of the scanned object directly from its projections on the detector, but a reconstruction process is needed. Besides, to achieve a high image resolution the pinholes need to be very close to the object to benefit from the high magnification factor. This might limit the effective arrangement of the pinholes around the object for sufficient angular sampling. In this case, images can still be reconstructed from an incomplete data set.

Several published works explored the idea of obtaining synthetic images from pinhole tomographic data with incomplete data sets (Wilson *et al* 2000, Havelin 2013, Havelin *et al* 2013). In these works, a multi-pinhole (MPH) collimator obtained projections at a number of pinhole–detector distances at a single tomographic angle, after which planar images were formed by summing three-dimensional (3D) reconstructions along the axis perpendicular to the collimator face.

Previously, we have tested patented technologies (Beekman 2011, 2014) in a breast scanner (van Roosmalen *et al* 2016) in which the pendant breast is lightly compressed between transparent Perspex plates and scanned between two sets of translating focusing MPH plates and gamma detectors. This forms angularly incomplete data sets that are then reconstructed to form images offering both 3D localisations of tracer uptakes and good tumour-to-background contrast-to-noise ratios.

The aim of the present work is to develop a method that is less sensitive to pinhole penetration in order to maintain high resolution (the ability to resolve small structures) with increasing photon energy. To this end, we develop a scanning focus nuclear microscope (SFNM) based on a focusing MPH concept with a target image resolution down to 40 μm for ^{99m}Tc. This device will be suitable for imaging small superficial structures in mice, for example, and for incubated tissue slices (Nonnekens *et al* 2016). This paper demonstrates *in silico* the performance of the new SFNM using Monte Carlo simulations to test several activity levels of ^{99m}Tc contained in a digital Derenzo phantom. A simulated bone scan of a mouse ankle was also assessed. The obtained images with SFNM were then compared with images generated using a single pinhole (SPH) with either matched pinhole diameter or matched sensitivity.

2. Methods

2.1. Scanning focus nuclear microscopy

The proposed SFNM imaging system consists of a focusing MPH collimator made of gold with a total of 42 round knife-edge pinholes, each having an opening angle of 10° (see figures 1(b), (c)). These 0.05 mm diameter pinholes focus on a 0.5 mm diameter central field of view (CFOV). The object is scanned through this focus to obtain data from various projection angles for each point in the object using a scanning focus method (Vastenhouw and Beekman 2007).

The MPH collimator has a rectangular shape with a wall thickness of 30 mm and can be mounted on a U-SPECT/CT or a VECTor/CT imaging system (MILabs B.V., the Netherlands) (van der Have *et al* 2009, Goorden *et al* 2013). It projects on one of the system's large-area gamma detectors (NaI(Tl) crystal). The gamma detector has a 3.5 mm intrinsic spatial resolution with 10% full width at half-maximum (FWHM) energy resolution at 140 keV (^{99m}Tc). The distances from the centre of the CFOV to the collimator's surface, to the pinhole's centre and to the detector's surface are 1.5 mm, 2 mm and 210 mm, respectively, which leads to a large pinhole magnification factor of 104.

For comparison with SFNM, we considered two SPH collimator designs (table 1), of which the CFOV size, collimator thickness and collimator-to-detector distance are the same as in SFNM (figure 1(a)). In the SPH1 design, we adjusted the pinhole diameter (0.35 mm) to match the sensitivity to that of the SFNM, whereas in the SPH2 design we set the pinhole diameter to the same value as that used in the SFNM (0.05 mm). The sensitivity was determined by Monte Carlo simulations (details in section 2.2) of a 0.3 mm thick disc-shaped uniform ^{99m}Tc activity distribution with the diameter of the CFOV. The disc lies in the *XY* plane. The sensitivity was then calculated by taking the fraction of the number of detected photons over the total number of photon emissions.

For the SPH designs, we both show direct detector projection (projected images) and reconstructed images obtained with the same scanning focus method as described for the SFNM (synthetic images).

2.2. Monte Carlo simulations

For the proposed SFNM system and SPH approach, simulation data were generated using the Monte Carlo Simulation package Geant4 Application for Tomographic Emission (GATE), version 8.0. The GATE application

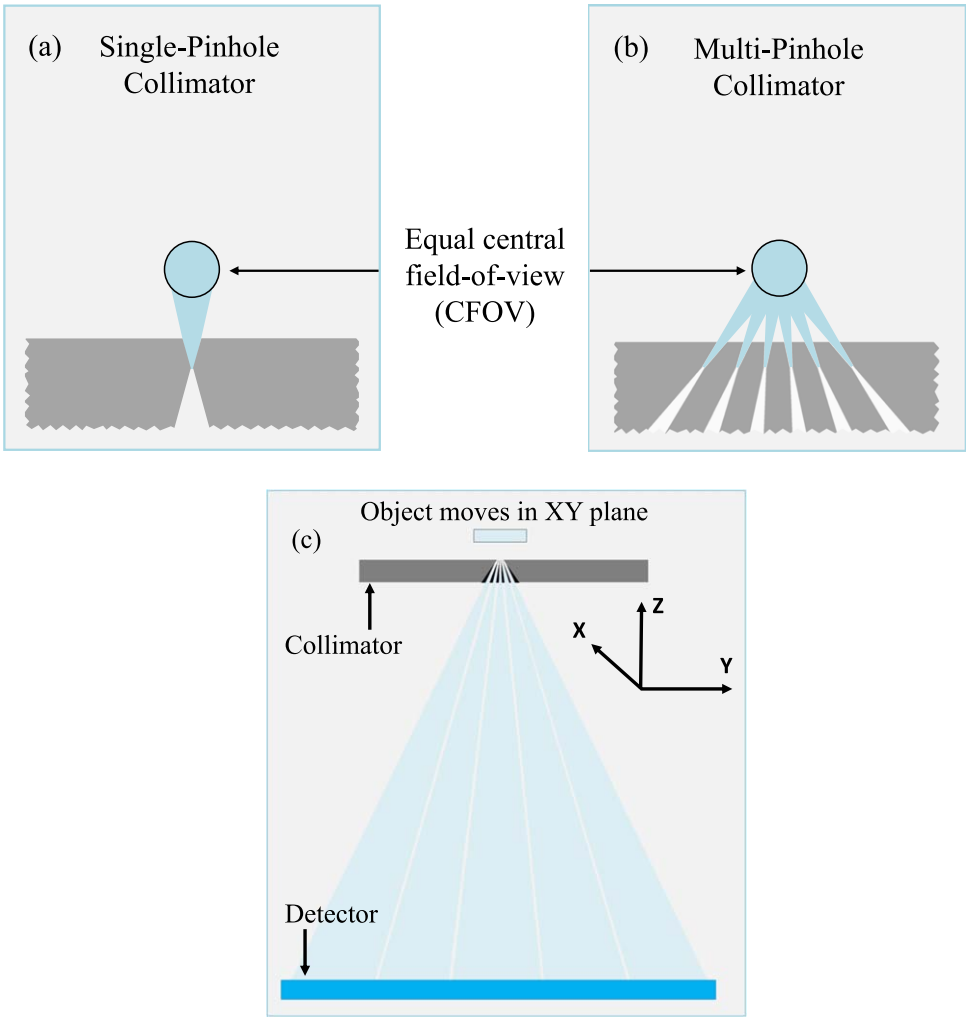

Figure 1. (a), (b) Illustration of the SPH and MPH collimators considered in this paper which were designed to have equal CFOVs. (c) The collimator is placed close to the object to achieve high magnification factors. The object is scanned at multiple positions in the *XY* plane.

Table 1. The SPH collimator designs that were evaluated in comparison with the SFNM.

	SPH1 (matched sensitivity)	**SPH2** (matched pinhole diameter)	**SFNM**
Pinhole diameter (mm)	0.35	0.05	0.05
Sensitivity (%)	0.13	0.010	0.13

was run in a CentOS 6.6 computer cluster with 250 processors running in parallel. To simulate photon paths through the collimator and in the detector, physics processes were defined by the 'physics list builder' mechanism in GATE, which includes but is not limited to photoelectric effect, Compton scatter, Rayleigh scatter, bremsstrahlung, electron ionisation and positron annihilation. To simulate the detector geometry, a NaI scintillator was created in GATE using a 497.4 mm $\times$ 410.6 mm $\times$ 9.5 mm rectangular box, which was placed as shown in figure 1(c).

STL files of the proposed focused MPH collimator and the SPH collimators were prepared using computer-aided design software (OpenSCAD), with the required pinhole diameter and collimator material. We assumed a MPH aperture made of gold to limit the pinhole edge penetration of gamma radiation. GATE outputs the total deposited energy in the scintillator and the interaction time of each gamma photon, along with the energy-weighted average interaction location in the scintillator. Photon interaction locations were sampled on a pixel grid with pixels of size 1.072 mm $\times$ 1.072 mm, the same as the pixel size of the real detectors used in the U-SPECT/CT or VECTor/CT imaging system (MILabs B.V., the Netherlands). The photopeak window was set to a 20% width at 140 keV.

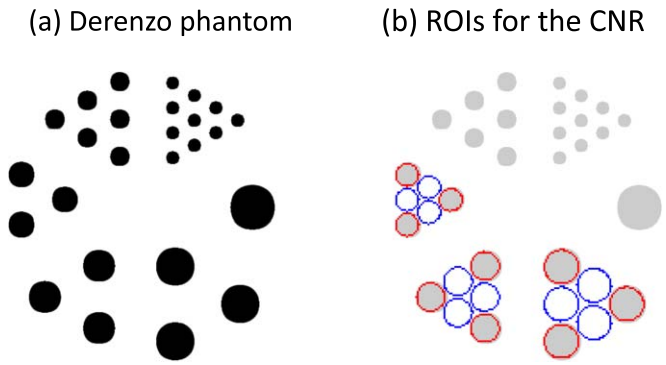

Figure 2. Derenzo phantom (a) and the regions of interest (ROIs) (b) for calculating contrast to noise ratios of the obtained images. The rod diameters are 0.07, 0.06, 0.05, 0.04, 0.03 and 0.02 mm.

2.3. Derenzo resolution phantom

The Derenzo resolution phantom simulated in this study has six sectors containing rod diameters ranging from 0.02 mm to 0.07 mm (figure 2). In each sector, the distance between the centres of two adjacent rods is twice the rod diameter. The rod length is 0.3 mm. The rods were defined in GATE using analytical cylinders, meaning that there was no voxelisation effect.

First, the phantom was simulated with SPH2 at one central bed position, assuming that it contained either 40 kBq of ^{125}I or ^{99m}Tc and that it was scanned for 2 h to assess the effect of increasing photon energy with this SPH.

Then, the phantom was simulated, assuming that it contained ^{99m}Tc at three activity levels (40 kBq, 8 kBq and 4 kBq in the whole phantom), and a 2 h acquisition was assumed. For the projected image with the SPH, the phantom was placed at the centre of CFOV and projections at a single position were acquired. For the synthetic images with both collimators, the Derenzo phantom was scanned at nine bed positions separated by a 0.25 mm step size in the *XY* plane.

2.4. Mouse ankle joint phantom

A mouse ankle joint phantom was derived from a real CT image of a mouse ankle joint having a voxel size of 0.08 mm. The mouse ankle phantom contained a realistic activity concentration of 336 MBq ml^{-1} of ^{99m}Tc, which we inferred from experimental mouse data (Nguyen *et al* 2020b). The phantom had a volume of 3.76 mm × 2.48 mm × 3.00 mm. For the synthetic images, the phantom was simulated assuming a scan time of either 1 h or 4 h and 693 bed positions separated by a 0.125 mm step in the *XY* plane. The time step was equal for all bed positions. For the projected image with the SPH for the comparison in figure 6, the area viewed by the pinhole at the centre of the system (0.5 mm diameter) is smaller than the phantom size; therefore, the mouse ankle phantom was moved in the *Z* direction 15 mm away from the pinhole such that the whole mouse ankle could be observed through the pinhole. In this case, the pinhole magnification is 13.5 times.

2.5. Image reconstruction and assessment

The acquired simulated projection data at multiple object positions were used collectively in image reconstruction. For image reconstruction, a system matrix was generated for the SFNM collimator using an in-house developed ray-tracing code that takes into account pinhole edge penetration and the spatial resolution and depth of interaction in the detector, but excludes scatter (Goorden *et al* 2016). For this ray-tracing simulation, the position, orientation and linear attenuation coefficients of the collimator (4.26 mm^{-1}) and detector (0.245 mm^{-1}) relevant for 140 keV energy were provided as input. To generate a reasonable system matrix size for fast image reconstruction, only the gamma photon paths that have at least a 4% probability of passing through the collimator material were included. A lower cut-off will lead to a matrix with many more elements, and a longer computation time for the matrix and image reconstruction. We found that for 140 keV, the cut-off of 4% resulted in approximately 96% of the photon flux being modelled, and this cut-off was sufficiently small in this case. Decay correction was included to account for the change in the activity in the object during the scan.

Images were reconstructed using a similarity-regulated ordered-subset expectation-maximisation (SROSEM) algorithm (Vaissier *et al* 2016) with the maximum number of subsets set to 128. All images presented in this work were reconstructed with a voxel size of 0.02 mm. A voxel size of 0.01 mm did not improve the resolution further but dramatically increased computation time; therefore, it was not used. Gaussian filters of 0.04 and 0.14 mm FWHM were applied to the reconstructed images of the Derenzo phantom and mouse ankle,

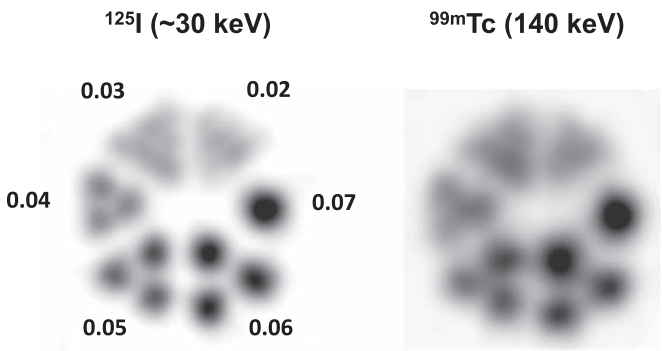

Figure 3. Simulated projection images of the Derenzo hot rod phantom with a single micro-pinhole showing the effect of increasing the photon energy. This was simulated for the SPH2 design. Rod diameters of the different sectors are provided in mm.

respectively. From these reconstructed images, synthetic planar images were generated by adding slices up to 0.3 mm and 3 mm for the Derenzo phantom and mouse ankle, respectively. The reconstruction iteration numbers were chosen to maximise the contrast-to-noise ratio (CNR; equations (1)–(2)) for the Derenzo images or to minimise the normalised root mean squared error (NRMSE) for the mouse ankle images.

Scatter correction was applied using the triple energy window method (Ogawa *et al* 1991) in a model-based approach (Bowsher *et al* 1992, King *et al* 1997). For this purpose, two side windows, each having a width equal to 25% of the width of the photopeak window, were set. The scatter estimate was then smoothed by a Gaussian filter having a standard deviation of five pixels and then added to the forward projection in each iteration during reconstruction.

For the SPH, the projection images shown in figures 4 and 6 were post-processed using Gaussian filters having FWHMs of 0.04 mm and 0.14 mm multiplied with a magnification factor of 104 and 13.5 for the Derenzo phantom and the mouse ankle joint phantom, respectively. The synthetic images with the SPH were obtained in the same way as with the SFNM. The obtained images were resampled with a 1.58 times smaller pixel size using bicubic interpolation and plotted with the pseudocolour ('pcolor') function in MATLAB to avoid a pixelation effect.

For the obtained resolution phantom image, CNR was calculated in the same way as in Walker *et al* (2014) by drawing regions of interest (ROIs) with red circles indicating the regions with activity and blue circles indicating the background regions (figure 2). ROIs had a diameter of 0.9 times the diameter of the rods. We defined the contrast (C_s) and noise (N_s) of rod sector s as follows:

$$C_s = \frac{\overline{I_s} - \overline{B_s}}{\overline{I_s}}, \tag{1}$$

$$N_s = \frac{\sqrt{\sigma_{I_s}^2 + \sigma_{B_s}^2}}{\overline{IB_s}}, \tag{2}$$

where $\overline{I_s}$ and $\overline{B_s}$ are the mean intensity over the activity regions (I_s) and background regions (B_s) of sector s, respectively. σ_{I_s} and σ_{B_s} are standard deviations over I_s and B_s, respectively, and $\overline{IB_s}$ is the mean intensity over all ROIs of sector s. Then the CNR of each rod sector was defined as C_s/N_s, and the average of the CNRs over sectors with 0.04, 0.05 and 0.06 mm diameter rods was taken as an image quality assessment (reported in figure 4). Sector 0.07 mm with only one rod and sectors 0.02 mm and 0.03 mm with non-discernible rods were excluded from this calculation.

3. Results

3.1. Derenzo resolution phantom

Figure 3 demonstrates the image degradation due to pinhole edge penetration when increasing the photon energy from 30 keV to 140 keV. Figure 4 shows the synthetically generated planar images of the Derenzo resolution phantom obtained by summing slices of the reconstructed images across the whole phantom length of 0.3 mm, as well as the projected images only for the SPH. The results show a clear advantage of SFNM over using a SPH collimator at a matched sensitivity. The achieved image resolution is 0.04 mm with SFNM, whereas in both the SPH projected and synthetic images with matched sensitivity the rods are not discernible. When compared at equal physical pinhole diameters, the improvement in image resolution by applying SFNM is still significant. In this case, the SFNM images contain far less background and image noise than the SPH2 projected

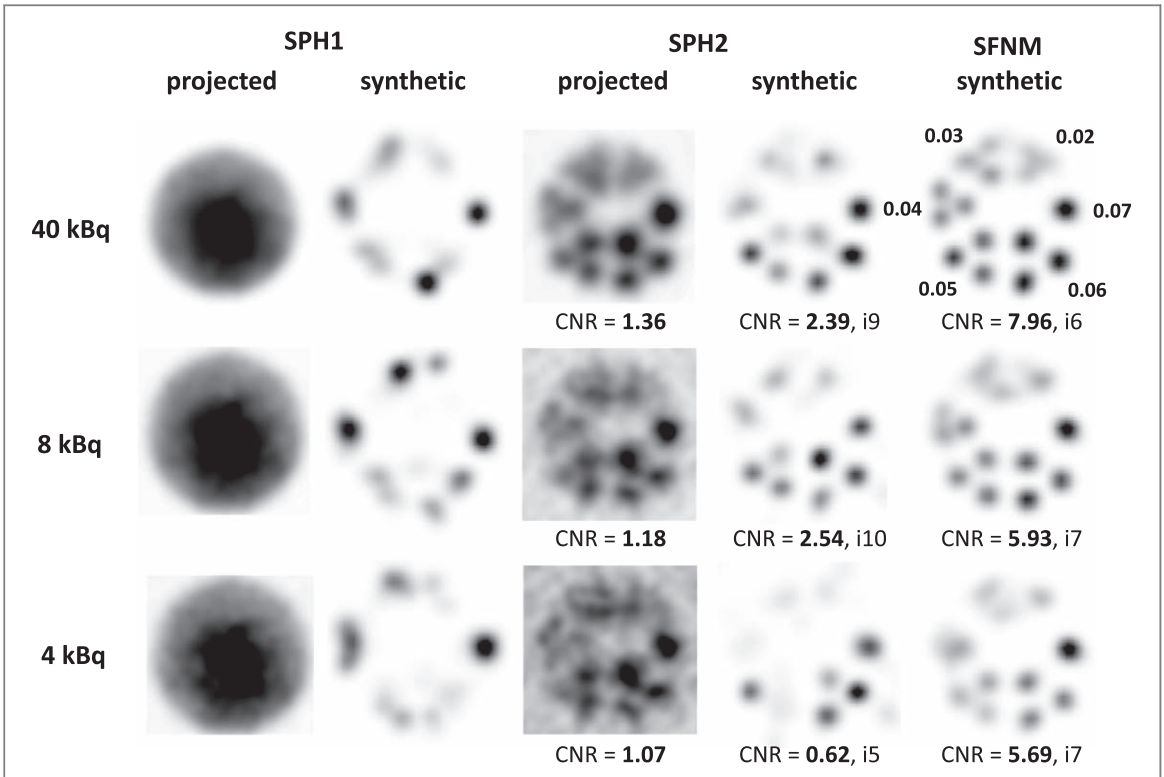

Figure 4. Derenzo resolution images generated with the proposed SFNM and the SPH camera with either matched sensitivity (SPH1) or matched pinhole diameter (SPH2) at equal dose. The CNRs for SPH2 and SFNM are listed underneath the images. For the synthetic images, if the CNR is listed, the corresponding reconstruction iteration number that maximised the CNR is also presented.

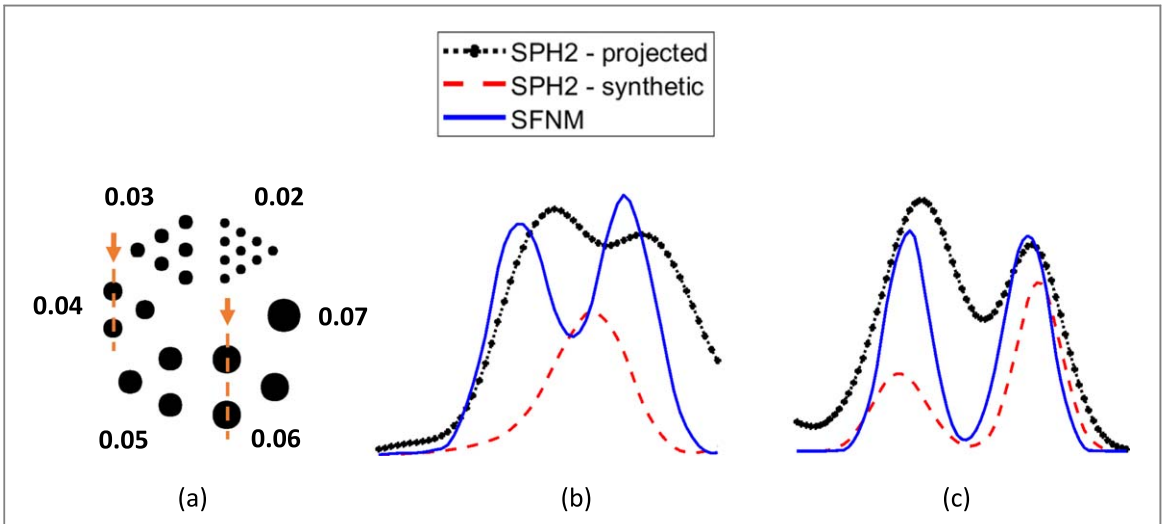

Figure 5. Profiles taken through different rod sectors obtained from the images in the first row (40 kBq) in figure 4 for SPH2 and SFNM. Locations of the profiles are indicated in (a). Profiles through the 0.04 mm rod sectors are shown in (b), while (c) shows profiles through the 0.06 mm rod sectors.

images, and visualise the rods better than the SPH2 synthetic images. This can also be seen on the profiles through different rod sectors (figure 5). The SFNM also gives the highest CNRs of the obtained Derenzo images among the presented methods.

3.2. Mouse ankle joint phantom

Figure 6 demonstrates the imaging capability of SFNM compared with the SPH cameras for the mouse ankle joint phantom. The synthetic image generated using SFNM clearly shows the anatomical structure of the mouse ankle and the best NRMSE among the presented methods.

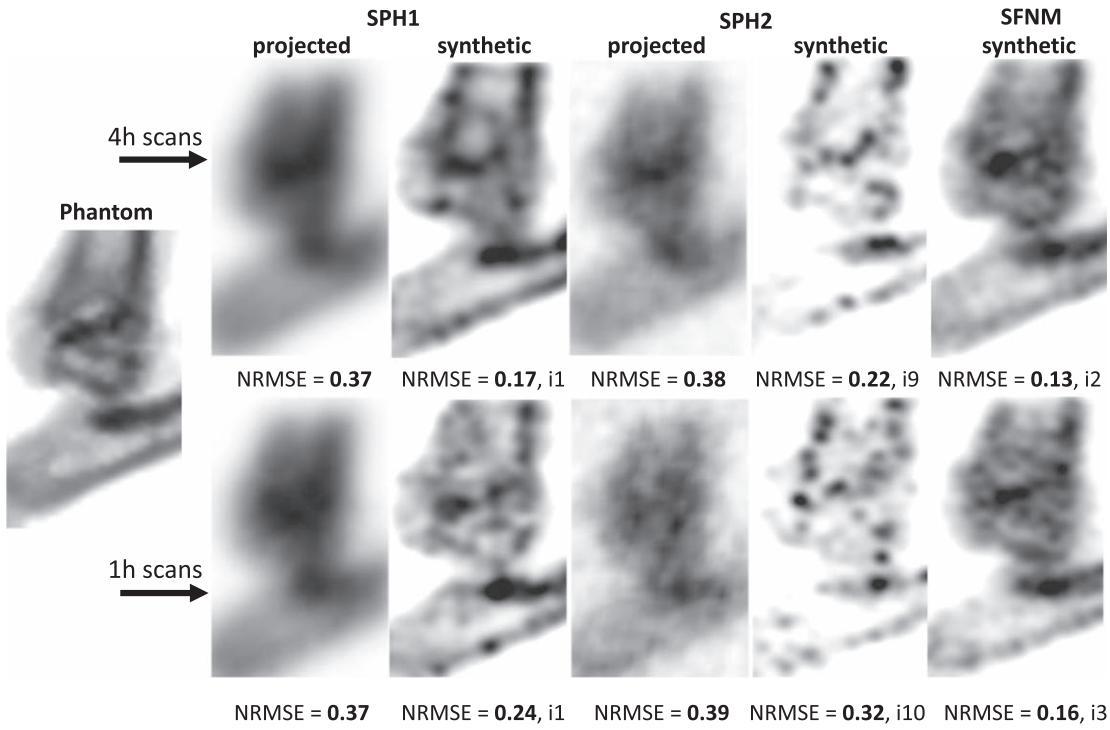

Figure 6. Mouse ankle joint images generated with the proposed SFNM and the SPH camera with either matched sensitivity (SPH1) or matched pinhole diameter (SPH2) at equal dose and scan time. The NRMSEs are listed underneath the images, and for the synthetic cases the reconstruction iteration number that minimised the NRMSE is also presented.

4. Discussion

This study proposes a new nuclear microscopic imaging method (scanning focus nuclear microscopy, SFNM) and investigates its projected performance *in silico*. The designed system generates synthetic planar images with a resolution of 0.04 mm for ^{99m}Tc.

In this work, a focused MPH collimator was used to reduce pinhole edge penetration for relatively high gamma energy radionuclide imaging, and it was shown to provide better image resolution and system sensitivity trade-off than obtained with SPH imaging. The results showed that at equal sensitivity (0.13%), the SPH did not resolve rods in the Derenzo phantom, whereas with SFNM a resolution of 0.04 mm was achieved. When compared at an equal pinhole diameter (0.05 mm), the improvement by applying SFNM is still significant and the SFNM images contain less background and image noise than the SPH projection, as well as higher resolution and CNR than the SPH synthetic images. An increase in the SPH diameter to obtain the same sensitivity as in the MPH case worsens the resolution more rapidly, whereas using an equal diameter to that in SFNM improves the resolution but at the cost of sensitivity, which decreased by more than 90%.

The mouse ankle joint phantom image showed that SFNM could be used for *in vivo* imaging. However, the sensitivity depends on the source–pinhole distance; therefore, the presented SFNM is most suitable for imaging small structures located close to the surface of the animals, such as subcutaneous or skin tumours, joints or the thyroid. In the future, biological tissue samples could also be investigated, for example tumour tissue slices stained with a tracer. This high-resolution device could provide information about tumour microvasculature, delivery and retention of drugs and other molecules targeted to the cancer cells. The ability of SFNM to image clinically relevant radionuclides such as ^{99m}Tc could lead to many *in vivo* diagnostic and therapeutic applications in the mouse that may be translated to the clinic.

The focused MPH collimator allowed us to acquire projection data from various projection angles, which could then be used to reconstruct 3D tomosynthesis images based on incomplete data. Later, planar synthetic images were generated by summing slices from reconstructed images. The limited angular sampling might cause artefacts in visualising large tissue slices. Also, because of the small field of view of the presented design, scanning a complete tissue slice will require many bed translations for a full sampling, which limits its use in dynamic imaging.

When manufacturing this MPH collimator, one possibility is to make a separate thin plate containing all the pinhole apertures placed above a collimator block containing all the pinhole ends, which together form a complete collimator. Although the simulations in this work assumed that the whole collimator was made of

gold, in reality we may use gold for only the pinhole plate because most of the pinhole penetration and scatter happens inside this part and the large block underneath can be made of another material such as tungsten. The pinhole plate is small enough to use pure gold or platinum or gold platinum alloys, for example (Beekman *et al* 2002). The majority of costs will be due to machining or other means of manufacture. Given that the pinhole diameter and opening angle are very small (0.05 mm and 10°, respectively), very high-precision methods will be needed to manufacture these pinhole plates.

Pinhole penetration can also be reduced by utilising keel-edge pinholes instead of knife-edge pinholes, as demonstrated by Accorsi and Metzler (2004), Van Der Have and Beekman (2006) and Van Audenhaege *et al* (2015); however, this advantage is smaller at larger angles of photon incidence, with significant loss of sensitivity. Accurate modelling of the penetration as part of the system matrix used in image reconstruction is also beneficial to improve imaging performance. That is why the synthetic images with the SPH were also substantially enhanced compared with the projection-only images.

5. Conclusion

We assessed a novel nuclear microscope design (SFNM) to produce synthetic pinhole images with unprecedented resolution (down to 0.04 mm). SFNM has strong advantages over other conventional high-resolution pinhole imaging approaches in terms of sensitivity, resolution and robustness to photon penetration.

Data availability statement

The data cannot be made publicly available upon publication because they contain commercially sensitive information. The data that support the findings of this study are available upon reasonable request from the authors.

ORCID iDs

Bart Oostenrijk https://orcid.org/0000-0001-6842-9004

References

Accorsi R and Metzler S D 2004 Analytic determination of the resolution-equivalent effective diameter of a pinhole collimator *IEEE Trans. Med. Imaging* **23** 750–63

Beekman F and Van Der Have F 2007 The pinhole: gateway to ultra-high-resolution three-dimensional radionuclide imaging *Eur. J. Nucl. Med. Mol. Imaging* **34** 151–61

Beekman F J 2014 Gamma radiation breast imaging apparatus *US Patent* 20140093035, NL2009566

Beekman F J 2011 Gamma radiation imaging apparatus *US Patent* 20110158384, EP2310876

Beekman F J, van der Have F, Vastenhouw B, van der Linden A J A, van Rijk P P, Burbach J P H and Smidt M P 2005 U-SPECT-I: a novel system for submillimeter-resolution tomography with radiolabeled molecules in mice *J. Nucl. Med.* **46** 1194–200

Beekman F J, McElroy D P, Berger F, Gambhir S S, Hoffman E J and Cherry S R 2002 Towards *in vivo* nuclear microscopy: iodine-125 imaging in mice using micro-pinholes *Eur. J. Nucl. Med.* **29** 933–8

Bowsher J E, Gilland D R, Floyd C E, Jaszczak R J, Johnson V E and Coleman R E 1992 Three-dimensional iterative reconstruction for SPECT *J. Nucl. Med.* **879**

Furenlid L R, Wilson D W, Chen Y C, Kim H, Pietraski P J, Crawford M J and Barrett H H 2004 FastSPECT II: a second-generation high-resolution dynamic SPECT imager *IEEE Trans. Nucl. Sci.* **51** 631–5

Goorden M C and Beekman F J 2010 High-resolution tomography of positron emitters with clustered pinhole SPECT *Phys. Med. Biol.* **55** 1265–77

Goorden M C, van der Have F, Kreuger R, Ramakers R M, Vastenhouw B, Burbach J P H, Booij J, Molthoff C F M and Beekman F J 2013 VECTor: a preclinical imaging system for simultaneous submillimeter SPECT and PET *J. Nucl. Med.* **54** 306–12

Goorden M C, van Roosmalen J, van der Have F and Beekman F J 2016 Optimising modelling in iterative image reconstruction for preclinical pinhole PET *Phys. Med. Biol.* **61** 3712–33

Havelin R 2013 Development of a high-resolution gamma-ray imaging system with synthetic collimation *PhD Thesis* National University of Ireland, Galway (https://www.researchgate.net/publication/262270772_Development_of_a_high-resolution_gamma-ray_imaging_system_with_synthetic_collimation)

Havelin R J, Miller B W, Barrett H H, Furenlid L R, Murphy J M, Dwyer R M and Foley M J 2013 Design and performance of a small-animal imaging system using synthetic collimation *Phys. Med. Biol.* **58** 3397

Hesterman J Y, Kupinski M A, Furenlid L R, Wilson D W and Barrett H H 2007 The multi-module, multi-resolution system (M3R): a novel small-animal SPECT system *Med. Phys.* **34** 987–93

Ivashchenko O, van der Have F, Villena J L, Groen H C, Ramakers R M, Weinans H H and Beekman F J 2014 Quarter-millimeter-resolution molecular mouse imaging with U-SPECT^{+} *Mol. Imaging* **14** 1–8

Kim H, Furenlid L R, Crawford M J, Wilson D W, Barber H B, Peterson T E, Hunter W C J, Liu Z, Woolfenden J M and Barrett H H 2006 SemiSPECT: a small-animal single-photon emission computed tomography (SPECT) imager based on eight cadmium zinc telluride (CZT) detector arrays *Med. Phys.* (https://doi.org/10.1118/1.2164070)

King M A, DeVries D J, Pan T, Pretorius P H and Case J A 1997 An investigation of the filtering of TEW scatter estimates used to compensate for scatter with ordered subset reconstructions *IEEE Trans. Nucl. Sci.* **44** 1140–5

Könik A, Auer B, De Beenhouwer J, Kalluri K, Zeraatkar N, Furenlid L R and King M A 2019 Primary, scatter, and penetration characterisations of parallel-hole and pinhole collimators for I-123 SPECT *Phys. Med. Biol.* **64** 1–27

Nguyen M P, Goorden M C and Beekman F J 2020a EXIRAD-HE: multi-pinhole high-resolution *ex vivo* imaging of high-energy isotopes *Phys. Med. Biol.* **65** 225029

Nguyen M P, Ramakers R M, Kamphuis C, Koustoulidou S, Goorden M C and Beekman F J 2020b EXIRAD-3D: Fast automated three-dimensional autoradiography *Nucl. Med. Biol.* **86–87** 59–65

Nonnekens J, van Kranenburg M, Beerens C E M T, Suker M, Doukas M, van Eijck C H J, de Jong M and van Gent D C 2016 Potentiation of peptide receptor radionuclide therapy by the PARP inhibitor olaparib *Theranostics* **6** 1821

Ogawa K, Harata Y, Ichihara T, Kubo A and Hashimoto S 1991 A practical method for position-dependent Compton-scatter correction in single photon emission CT *IEEE Trans. Med. Imaging* **10** 408–12

Sánchez F *et al* 2013 ALBIRA: a small animal PET/SPECT/CT imaging system *Med. Phys.* **40** 051906

Schramm N, Hoppin J, Lackas C, Forrer F, Valkema R and de Jong M 2006 The NanoSPECT: a high-sensitivity multi-pinhole SPECT system with submillimeter (nanoliter) spatial resolution for imaging small rodents *J. Nucl. Med.* **47** 233P

Van Audenhaege K, Van Holen R, Vandenberghe S, Vanhove C, Metzler S D and Moore S C 2015 Review of SPECT collimator selection, optimisation, and fabrication for clinical and preclinical imaging *Med. Phys.* **42** 4796–813

Van Der Have F and Beekman F J 2006 Penetration, scatter and sensitivity in channel micro-pinholes for SPECT: a Monte Carlo investigation *IEEE Trans. Nucl. Sci.* **53** 2635–45

van der Have F, Vastenhouw B, Ramakers R M, Branderhorst W, Krah J O, Ji C, Staelens S G and Beekman F J 2009 U-SPECT-II: an ultra-high-resolution device for molecular small-animal imaging *J. Nucl. Med.* **50** 599–605

van Roosmalen J, Goorden M C and Beekman F J 2016 Molecular breast tomosynthesis with scanning focus multi-pinhole cameras *Phys. Med. Biol.* **61** 5508–28

Vaissier P E B, Beekman F J and Goorden M C 2016 Similarity-regulation of OS-EM for accelerated SPECT reconstruction *Phys. Med. Biol.* **61** 4300–15

Vastenhouw B and Beekman F 2007 Submillimeter total-body murine imaging with U-SPECT-I *J. Nucl. Med.* **48** 487–93

Walker M D, Goorden M C, Dinelle K, Ramakers R M, Blinder S, Shirmohammad M, van der Have F, Beekman F J and Sossi V 2014 Performance assessment of a preclinical PET scanner with pinhole collimation by comparison to a coincidence-based small-animal PET scanner *J. Nucl. Med.* **55** 1368–74

Wilson D W, Barrett H H and Clarkson E W 2000 Reconstruction of two- and three-dimensional images from synthetic-collimator data *IEEE Trans. Med. Imaging* **19** 412–22